Transient Stability Analysis of Mixed GFM-GFL Inverter System Based on Contraction Theory

Yingyi Tang
Thayer School of Engineering
Dartmouth College
Hanover, New Hampshire, USA
e-mail: yingyi.tang.th@dartmouth.edu

Junbo Zhao
Thayer School of Engineering
Dartmouth College
Hanover, New Hampshire, USA
e-mail: junbo.zhao@dartmouth.edu

Baosen Zhang
Electrical & Computer Engineering
University of Washington
Seattle, Washington, USA
e-mail: zhangbao@uw.edu

***Abstract*—The integration of both grid-forming (GFM) and grid-following (GFL) inverters introduces significant complexity into system dynamics, posing challenges for transient stability analysis in modern power systems. This paper investigates the transient stability of mixed GFM–GFL-inverter systems from a novel perspective based on contraction theory. The transient stability is examined incrementally through the displacement between neighboring trajectories. A state-dependent contraction metric is proposed based on system's dynamic Jacobian matrix and the corresponding contraction region is derived. Numerical results verify the effectiveness of the proposed method and demonstrate that the state-dependent metric provides less conservative contraction regions compared with constant metric.**

***Index Terms*—Mixed GFM-GFL-inverter system, transient stability, contraction theory, state-dependent metric, contraction region.**

I. Introduction

Inverters are essential for applications such as the integration of renewable resources [1]. These inverters primarily operate using either grid-following (GFL) or grid-forming (GFM) control strategies [2]. While the dominant GFL control could efficiently control the injected current, the GFM scheme emulates a voltage source to provide grid support [3], [4]. Given their complementary strengths, mixed systems combining both GFM and GFL inverters are anticipated to be a key architecture for future power grids [5]. However, the mixed GFM-GFL-inverter systems exhibit highly nonlinear and intricate dynamics [6], which poses a significant challenge to transient stability analysis.

Recent studies have explored transient stability of mixed GFM-GFL inverter systems through various approaches such as phase portrait methods, equal area criterion (EAC), and Lyapunov approaches. Phase portrait analyses revealed that the variation of the GFM-inverter terminal voltage would lead to the change of the GFL-inverter power angle [7], and interactions among inverters would benefit GFL but destabilize GFM inverters [8]. Yet, the phase portrait remains a numerical tool, which limits its ability to provide clear parameter-level understanding. EAC-based studies demonstrated that GFL current injection could suppress GFM output under large disturbances [9] and angle-difference regulation strategies were proposed accordingly [10]. However, the EAC method's positive damping assumption cannot fully capture PLL-induced negative damping effects. While [11] estimated stability regions using Lyapunov methods with Takagi-Sugeno fuzzy models, the lack of analytical expressions limited parameter impact assessment to iterative approaches.

This work is partially supported by the U.S. Department of Energy Office of Electricity. 979-8-3315-8138-1

Due to the aforementioned limitations of traditional stability analysis methods, we employ contraction theory to investigate the transient stability of mixed GFM-GFL-inverter systems, an approach rarely applied to inverter-dominated systems. Contraction theory offers a fundamentally different approach for stability analysis of nonlinear systems. Unlike Lyapunov theory, contraction theory analyzes stability incrementally by examining whether nearby trajectories converge to one another [12]. This differential approach has proven effective in network system stability and synchronization [13], as well as in robust stability analysis of uncertain systems using convex optimization and sum of squares programming [14].

For power systems, a critical question is whether system trajectories converge to the stable equilibrium point (SEP). According to contraction theory, within a contraction region containing an SEP, any two neighboring trajectories would eventually converge to that SEP, which is referred to as the attraction set [15]. A constant metric for contraction analysis of conventional power systems was proposed in [16], through which the corresponding contraction region was derived. In contrast, for inverter-dominated systems, contraction region analysis has not yet been explored. In this work, we propose a systematic contraction region analysis framework for mixed GFM–GFL inverter systems. The main contributions are summarized as follows:

1) A mathematical model of the mixed GFM-GFL-inverter system for transient stability analysis is established.

2) A state-dependent contraction metric is proposed for the mixed GFM–GFL inverter system, derived based on the structure of the dynamic Jacobian matrix. The corresponding contraction region is subsequently obtained via contraction theory.

Numerical results validate the effectiveness of the proposed method, showing that the state-dependent metric is less conservative than the constant metric.

II. Dynamic System Modelling

A. AC Network Modelling and Reference Frames

As shown in Fig. 1, n GFL inverters (Bus $1 \sim$ Bus n) and m GFM inverters (Bus $n+1 \sim$ Bus $n+m$) are connected in a power network. We assume the synchronous generator at Bus $n+m+1$ has comparably large inertia and is thereby treated as an infinite voltage source with value $U_g e^{j\theta_g}$. We assume that there are also k interior non-sourced buses (Bus $n+m+2 \sim$ Bus $n+m+k+1$) in the network. Regarding the boundaries buses (subscript $\boldsymbol{\alpha}$) and the interior buses (subscript $\boldsymbol{\beta}$), the interior nodes are eliminated by Kron reduction, yielding the reduced admittance matrix as

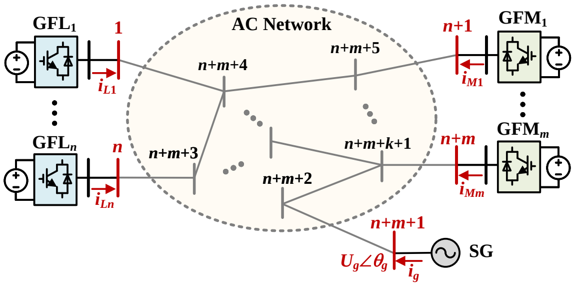

Fig. 1. Transmission system incorporated with mixed GFM and GFL inverters.

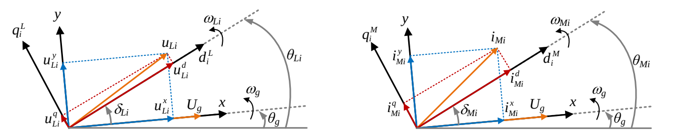

(a) GFL rotating reference frames (b) GFM rotating reference frames

Fig. 2. xy rotating reference frames and inverters dq rotating reference frames.

$\mathbf{Y_{new}} = \mathbf{Y}_{\boldsymbol{\alpha}} - \mathbf{Y}_{\boldsymbol{\alpha\beta}}\mathbf{Y}_{\boldsymbol{\beta}}^{-1}\mathbf{Y}_{\boldsymbol{\beta\alpha}} \in \mathbb{R}^{(n+m)\times(n+m)}$. Partitioning $\mathbf{Y_{new}}$ yields

$$\begin{bmatrix}\mathbf{i_L}\\ \mathbf{i_M}\\ i_g\end{bmatrix} = \mathbf{Y_{new}}\begin{bmatrix}\mathbf{u_L}\\ \mathbf{u_M}\\ u_g\end{bmatrix} = \begin{bmatrix}\mathbf{Y_L} & \mathbf{Y_{LM}} & \mathbf{Y_{Lg}}\\ \mathbf{Y_{ML}} & \mathbf{Y_M} & \mathbf{Y_{Mg}}\\ \mathbf{Y_{gL}} & \mathbf{Y_{gM}} & \mathbf{Y_g}\end{bmatrix}\begin{bmatrix}\mathbf{u_L}\\ \mathbf{u_M}\\ u_g\end{bmatrix} \tag{1}$$

where $\mathbf{i_L},\ \mathbf{u_L} \in \mathbb{R}^{n\times 1}$ and $\mathbf{i_M},\ \mathbf{u_M} \in \mathbb{R}^{m\times 1}$ denote the point of common coupling (PCC) currents and voltages of GFL and GFM inverters, respectively. i_g, u_g are the current and voltage of the infinite bus.

As shown in Fig. 2, the common xy reference frame of the network rotates at ω_g (1 p.u.), whereas the local dq frames of the i-th GFL and GFM inverters rotate at ω_{Li} and ω_{Mi}, respectively. Their power angles are defined relative to the infinite bus as

$$\delta_{Li} = \theta_{Li} - \theta_g, \quad \delta_{Mi} = \theta_{Mi} - \theta_g \tag{2}$$

where θ_g, θ_{Li} and θ_{Mi} are the angles of the infinite bus, the i-th GFL inverter and the i-th GFM inverter, respectively. Aligning the x-axis with the infinite bus voltage $U_g e^{j\theta_g}$ yields

$$u_g = U_g e^{j\theta_g}, \quad i_g = (i_g^x + j i_g^y)e^{j\theta_g}. \tag{3}$$

The voltage and current for the i-th GFL inverter and the i-th GFM inverter in local dq rotating frames are expressed as

$$\begin{cases}\mathbf{i}_{\mathbf{L}(i)} = (i_{Li}^d + j i_{Li}^q)e^{j\theta_{Li}} = I_{Li}e^{j(\theta_{Li}+\phi_{Li})}\\ \mathbf{u}_{\mathbf{M}(i)} = (u_{Mi}^d + j u_{Mi}^q)e^{j\theta_{Mi}} = U_{Mi}e^{j\theta_{Mi}}\end{cases} \tag{4}$$

$$\mathbf{u}_{\mathbf{L}(i)} = (u_{Li}^d + j u_{Li}^q)e^{j\theta_{Li}}, \mathbf{i}_{\mathbf{M}(i)} = (i_{Mi}^d + j i_{Mi}^q)e^{j\theta_{Mi}} \tag{5}$$

where $\phi_{Li} = \arctan(i_{Li}^q / i_{Li}^d)$ and the GFL inverters' current magnitudes and the GFM inverters' voltage magnitudes are assumed to remain at their reference values: $\left|\mathbf{i}_{\mathbf{L}(i)}\right| = I_{Li}$, $\left|\mathbf{u}_{\mathbf{M}(i)}\right| = U_{Mi}$.

B. Dynamic Model of Coupled GFM and GFL Inverters

In the studied system, synchronization loops of the GFL and GFM inverters employ PLL control and VSG control, respectively. Their synchronization mechanisms are described by

$$\begin{cases}\dot{\delta}_{Li} = \omega_b \cdot \bar{\omega}_{Li}\\ \dot{\bar{\omega}}_{Li} = K_{\mathrm{P}i}^{\mathrm{PLL}}\dot{u}_{Li}^q + K_{\mathrm{I}i}^{\mathrm{PLL}}u_{Li}^q\end{cases} \tag{6}$$

$$\begin{cases}\dot{\delta}_{Mi} = \omega_b \cdot \bar{\omega}_{Mi}\\ \dot{\bar{\omega}}_{Mi} = (P_{Mi}^{\mathrm{ref}} - P_{Mi})/J_i - (D_i/J_i)\cdot\bar{\omega}_{Mi}\end{cases} \tag{7}$$

where $\bar{\omega}_{Li} = \omega_{Li} - \omega_g$ and $\bar{\omega}_{Mi} = \omega_{Mi} - \omega_g$. $K_{\mathrm{P}i}^{\mathrm{PLL}}$ and $K_{\mathrm{I}i}^{\mathrm{PLL}}$ are the proportional and integral gains of the i-th GFL inverter's PLL control, respectively. P_{Mi}^{ref}, J_i and D_i denote the reference active power, virtual inertia and damping coefficient of the i-th GFM inverter, respectively. Its active power P_{Mi} is calculated by $P_{Mi} = U_{Mi}^d i_{Mi}^d + U_{Mi}^q i_{Mi}^q = U_{Mi}^d i_{Mi}^d$, where the q-axis voltage reference of GFM inverters is normally set to zero.

Based on (1), the voltages of GFL inverters and the currents of GFM inverters are derived as

$$\begin{cases}\mathbf{u_L} = \mathbf{A_1 i_L} - \mathbf{A_2 u_M} - \mathbf{A_3}u_g\\ \mathbf{i_M} = \mathbf{B_1 i_L} - \mathbf{B_2 u_M} - \mathbf{B_3}u_g\end{cases} \tag{8}$$

where $\mathbf{A_1} = \mathbf{Y_L^{-1}}$, $\mathbf{A_2} = \mathbf{Y_L^{-1}Y_{LM}}$, $\mathbf{A_3} = \mathbf{Y_L^{-1}}Y_{\mathbf{Lg}}$, $\mathbf{B_1} = \mathbf{Y_{ML}Y_L^{-1}}$, $\mathbf{B_2} = \mathbf{Y_M} - \mathbf{Y_{ML}Y_L^{-1}Y_{LM}}$, and $\mathbf{B_3} = \mathbf{Y_{Mg}} - \mathbf{Y_{ML}Y_L^{-1}Y_{Lg}}$. Based on network coupling, (8) relates $\mathbf{u_L}$ and $\mathbf{i_M}$ to the elements $\mathbf{i_L}$ and $\mathbf{u_M}$, whose magnitudes are fixed as defined in (4).

Substituting (2)-(5) into (8) yields

$$\begin{aligned}(u_{Li}^d + j u_{Li}^q)e^{j\delta_{Li}} = \sum\nolimits_{j=1}^{n}\mathbf{A_{1}}_{(i,j)}I_{Lj}e^{j(\phi_{Lj}+\delta_{Lj})} - \\ \sum\nolimits_{j=1}^{m}\mathbf{A_{2}}_{(i,j)}U_{Mj}e^{j\delta_{Mj}} - \mathbf{A_{3}}_{(i)}U_g\end{aligned} \tag{9}$$

$$\begin{aligned}(i_{Mi}^d + j i_{Mi}^q)e^{j\delta_{Mi}} = \sum\nolimits_{j=1}^{n}\mathbf{B_{1}}_{(i,j)}I_{Lj}e^{j(\phi_{Lj}+\delta_{Lj})} + \\ \sum\nolimits_{j=1}^{m}\mathbf{B_{2}}_{(i,j)}U_{Mj}e^{j\delta_{Mj}} + \mathbf{B_{3}}_{(i)}U_g.\end{aligned} \tag{10}$$

Define $\theta_{Lj} = \phi_{Lj} + \delta_{Lj}$, $\theta_{Mj} = \delta_{Mj}$, $\theta_g = 0$. For the subscriptions, we define the index $\mathcal{L}_i$ and $\mathcal{M}_i$ as $\mathcal{L}_i = \{L_j : j = 1,...,n,\ j \neq i\} \cup \{M_j : j = 1,...,m\} \cup \{g\}$ and $\mathcal{M}_i = \{L_j : j = 1,...,n\} \cup \{M_j : j = 1,...,m,\ j \neq i\} \cup \{g\}$.

By substituting (9) into (6) and (10) into (7), the GFL and GFM inverters' dynamics can be rewritten as

$$\begin{cases}\dot{\delta}_{Li} = \omega_b \cdot \bar{\omega}_{Li}\\ \dot{\delta}_{Mi} = \omega_b \cdot \bar{\omega}_{Mi}\\ \dot{\bar{\omega}}_{Li} = K_{\mathrm{I}i}^{\mathrm{PLL}}C_{u_{Li}}^q + K_{\mathrm{I}i}^{\mathrm{PLL}}\sum\limits_{r\in\mathcal{L}_i}\begin{bmatrix}\alpha_r\cos(\delta_{Li}-\theta_r) - \\ \beta_r\sin(\delta_{Li}-\theta_r)\end{bmatrix} - \\ \qquad K_{\mathrm{P}i}^{\mathrm{PLL}}\omega_b\sum\limits_{r\in\mathcal{L}_i}\begin{bmatrix}\alpha_r\sin(\delta_{Li}-\theta_r) + \\ \beta_r\cos(\delta_{Li}-\theta_r)\end{bmatrix}\cdot(\bar{\omega}_{Li}-\bar{\omega}_r)\\ \dot{\bar{\omega}}_{Mi} = \dfrac{P_{Mi}^{\mathrm{ref}} - U_{Mi}C_{i_{Mi}}^d}{J_i} - \dfrac{U_{Mi}}{J_i}\sum\limits_{r\in\mathcal{M}_i}\begin{bmatrix}\mu_r\cos(\delta_{Mi}-\theta_r) - \\ \nu_r\sin(\delta_{Mi}-\theta_r)\end{bmatrix}\\ \qquad -(D_i/J_i)\cdot\bar{\omega}_{Mi}\end{cases} \tag{11}$$

where for $r \in \mathcal{L}_i$:

$$\begin{cases}C_{u_{Li}}^q = I_{Li}\left(\mathbf{A}_{1(i,i)}^{\mathrm{Im}}\cos\phi_{Li} + \mathbf{A}_{1(i,i)}^{\mathrm{Re}}\sin\phi_{Li}\right)\\ \alpha_{L_j} = I_{Lj}\mathbf{A}_{1(i,j)}^{\mathrm{Im}}, \quad \beta_{L_j} = I_{Lj}\mathbf{A}_{1(i,j)}^{\mathrm{Im}}\\ \alpha_{M_j} = -U_{Mj}\mathbf{A}_{2(i,j)}^{\mathrm{Im}}, \quad \beta_{M_j} = -U_{Mj}\mathbf{A}_{2(i,j)}^{\mathrm{Re}}\\ \alpha_g = -U_g\mathbf{A}_{3(i)}^{\mathrm{Im}}, \quad \beta_g = -U_g\mathbf{A}_{3(i)}^{\mathrm{Re}}.\end{cases} \tag{12}$$

And for $r \in \mathcal{M}_i$:

$$\begin{cases}C_{i_{Mi}}^d = U_{M_i}\mathbf{B}_{2(i,i)}^{\mathrm{Re}}\\ \mu_{L_j} = I_{Lj}\mathbf{B}_{\mathbf{1}(i,j)}^{\mathrm{Re}}, \quad \nu_{L_j} = -I_{Lj}\mathbf{B}_{\mathbf{1}(i,j)}^{\mathrm{Im}}\\ \mu_{M_j} = U_{Mj}\mathbf{B}_{2(i,j)}^{\mathrm{Re}}, \quad \nu_{M_j} = -U_{Mj}\mathbf{B}_{2(i,j)}^{\mathrm{Im}}\\ \mu_g = U_g\mathbf{B}_{3(i,j)}^{\mathrm{Re}}, \quad \nu_g = -U_g\mathbf{B}_{3(i,j)}^{\mathrm{Im}}.\end{cases} \tag{13}$$

The dynamic model of the mixed GFM-GFL-inverter system is established by (11)-(13). It can be observed that the system is highly nonlinear and exhibits significant coupling between its state variables.

979-8-3315-8138-1

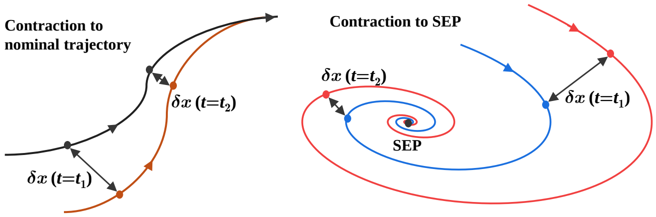

(a) δx dynamics in scenario 1 (b) δx dynamics in scenario 2

Fig. 3. Illustration of $\delta \mathbf{x}$ evolution in contraction theory.

III. Transient Stability Analysis via Contraction Theory

A. Contraction Theory

Contraction theory is a stability theory for nonlinear systems, in which stability is investigated incrementally between two arbitrary trajectories. The main concepts of contraction theory are summarized as follows.

Consider the nonlinear dynamic system

$$\dot{\mathbf{x}} = \mathbf{f}(\mathbf{x}). \tag{14}$$

By defining $\delta\mathbf{x}$ as the virtual displacement in the state $\mathbf{x}$, the system differential dynamics are introduced as $\delta\dot{\mathbf{x}} = \frac{\partial \mathbf{f}(\mathbf{x})}{\partial \mathbf{x}}\delta\mathbf{x} = \mathbf{J}(\mathbf{x})\delta\mathbf{x}$. The norm of $\delta\mathbf{x}$ measures the distance to the original trajectory, and the derivative of the norm squared value is given by

$$\frac{d}{dt}(\delta\mathbf{x}^\top\delta\mathbf{x}) = 2\delta\mathbf{x}^\top\mathbf{J}(\mathbf{x})\delta\mathbf{x}. \tag{15}$$

If $\mathbf{J}(\mathbf{x})$ is negative definite, the Euclidean length of $\delta\mathbf{x}$ would decrease over time and indicate the convergence of the neighboring trajectories to either a single trajectory or to a SEP (see Fig. 3).

A linear transformation of $\delta\mathbf{x}$ between two neighboring trajectories is introduced as

$$\delta\mathbf{z} = \mathbf{\Theta}(\mathbf{x})\delta\mathbf{x}. \tag{16}$$

This leads to a generalization of the distance to

$$\delta\mathbf{z}^\top\delta\mathbf{z} = \delta\mathbf{x}^\top\mathbf{\Theta}(\mathbf{x})^\top\mathbf{\Theta}(\mathbf{x})\delta\mathbf{x} = \delta\mathbf{x}^\top\mathbf{M}(\mathbf{x})\delta\mathbf{x} \tag{17}$$

where $\mathbf{M}(\mathbf{x})$ represents a state-dependent metric for the virtual displacement. Then the generalized squared distance's time derivative can be computed as

$$\frac{d}{dt}(\delta\mathbf{x}^\top\mathbf{M}(\mathbf{x})\delta\mathbf{x}) = \delta\mathbf{x}^\top\begin{pmatrix}\mathbf{J}(\mathbf{x})^\top\mathbf{M}(\mathbf{x}) + \\ \mathbf{M}(\mathbf{x})\mathbf{J}(\mathbf{x}) + \dot{\mathbf{M}}(\mathbf{x})\end{pmatrix}\delta\mathbf{x}. \tag{18}$$

Accordingly, convergence of two neighboring trajectories can be concluded in regions of $(\mathbf{J}(\mathbf{x})^\top\mathbf{M}(\mathbf{x}) + \mathbf{M}(\mathbf{x})\mathbf{J}(\mathbf{x}) + \dot{\mathbf{M}}(\mathbf{x})) \prec 0$. The corresponding region Ω is referred as the contraction region.

It is worth noting that for a constant metric $\mathbf{M}(\mathbf{x}) = \mathbf{M}$, where $\dot{\mathbf{M}}(\mathbf{x}) = 0$, the analysis reduces to Krasovskii's method in the Lyapunov stability framework [17].

B. Dynamic Jacobian Matrix for the Mixed GFM-GFL System

Based on the mixed GFM-GFL system dynamic model established in (11), the system dynamics can be organized as

$$\begin{cases}\mathbf{x} = [\delta_\mathbf{L},\ \delta_\mathbf{M},\ \bar{\omega}_\mathbf{L},\ \bar{\omega}_\mathbf{M}]^\top \\ \mathbf{f}(\mathbf{x}) = [\omega_b\bar{\omega}_\mathbf{L},\ \omega_b\bar{\omega}_\mathbf{M},\ \mathbf{f}_{\bar{\omega}_\mathbf{L}},\ \mathbf{f}_{\bar{\omega}_\mathbf{M}}]^\top\end{cases} \tag{19}$$

where $\delta_\mathbf{L} = [\delta_{L1},\cdots,\delta_{Ln}]^\top$, $\delta_\mathbf{M} = [\delta_{M1},\cdots,\delta_{Mm}]^\top$, $\bar{\omega}_\mathbf{L} = [\bar{\omega}_{L1},\cdots,\bar{\omega}_{Ln}]^\top$ and $\bar{\omega}_\mathbf{M} = [\bar{\omega}_{M1},\cdots,\bar{\omega}_{Mm}]^\top$. The i-th element of $\mathbf{f}_{\bar{\omega}_\mathbf{L}} \in \mathbb{R}^{n\times 1}$ and the i-th element of $\mathbf{f}_{\bar{\omega}_\mathbf{M}} \in \mathbb{R}^{m\times 1}$ are define by the third and the fourth terms of (11), respectively.

The dynamic Jacobian matrix of the system is accordingly derived as

$$\mathbf{J} = \frac{\partial \mathbf{f}(\mathbf{x})}{\partial \mathbf{x}} = \begin{bmatrix}\mathbf{0} & \omega_b\mathbf{I}_{n+m} \\ \mathbf{J}_{\bar{\omega},\delta} & \mathbf{J}_{\bar{\omega},\bar{\omega}}\end{bmatrix} \tag{20}$$

where

$$\mathbf{J}_{\bar{\omega},\delta} = \begin{bmatrix}\mathbf{J}_{\bar{\omega}_L,\delta_L} & \mathbf{J}_{\bar{\omega}_L,\delta_M} \\ \mathbf{J}_{\bar{\omega}_M,\delta_L} & \mathbf{J}_{\bar{\omega}_M,\delta_M}\end{bmatrix}, \quad \mathbf{J}_{\bar{\omega},\bar{\omega}} = \begin{bmatrix}\mathbf{J}_{\bar{\omega}_L,\bar{\omega}_L} & \mathbf{J}_{\bar{\omega}_L,\bar{\omega}_M} \\ 0_{m\times n} & -\mathbf{D}_\mathbf{J}\end{bmatrix} \tag{21}$$

and $\mathbf{D}_\mathbf{J} = \mathrm{diag}(D_1/J_1,\cdots,D_m/J_m)$. Define the control parameter matrices as $\mathbf{K}_\mathrm{P}^\mathrm{PLL} = \mathrm{diag}(K_{\mathrm{P}1}^\mathrm{PLL},\cdots,K_{\mathrm{P}n}^\mathrm{PLL})$, $\mathbf{K}_\mathrm{I}^\mathrm{PLL} = \mathrm{diag}(K_{\mathrm{I}1}^\mathrm{PLL},\cdots,K_{\mathrm{I}n}^\mathrm{PLL})$, $\mathbf{J}_\mathbf{M} = \mathrm{diag}(J_1,\cdots,J_m)$. Define

$$\begin{cases} g_{ir} = -\alpha_r\sin(\delta_{Li}-\theta_r) - \beta_r\cos(\delta_{Li}-\theta_r) \\ k_{ir} = -\mu_r\sin(\delta_{Mi}-\theta_r) - \nu_r\cos(\delta_{Mi}-\theta_r).\end{cases} \tag{22}$$

Then the sub-matrices in (21) are detailed as

$$\begin{cases}\mathbf{J}_{\bar{\omega}_L,\delta_L} = \omega_b\mathbf{K}_\mathrm{P}^\mathrm{PLL}\left(\mathrm{diag}(\dot{\mathcal{W}}^{LL}\mathbf{1}_n) - \dot{\mathcal{W}}^{LL}\right) + \\ \qquad \mathbf{K}_\mathrm{I}^\mathrm{PLL}\left(\mathrm{diag}(\mathcal{W}^{LL}\mathbf{1}_n) - \mathcal{W}^{LL}\right) \\ \mathbf{J}_{\bar{\omega}_L,\delta_M} = -\omega_b\mathbf{K}_\mathrm{P}^\mathrm{PLL}\dot{\mathcal{W}}^{LM} - \mathbf{K}_\mathrm{I}^\mathrm{PLL}\mathcal{W}^{LM} \\ \mathbf{J}_{\bar{\omega}_M,\delta_L} = -\mathbf{J}_\mathbf{M}{}^{-1}\mathbf{U}_\mathbf{M}\mathcal{W}^{ML} \\ \mathbf{J}_{\bar{\omega}_M,\delta_M} = -\mathbf{J}_\mathbf{M}{}^{-1}\mathbf{U}_\mathbf{M}\left(\mathrm{diag}(\mathcal{W}^{MM}\mathbf{1}_m) - \mathcal{W}^{MM}\right)\end{cases} \tag{23}$$

$$\begin{cases} J_{\bar{\omega}_L,\bar{\omega}_L} = \omega_b\mathbf{K}_\mathrm{P}^\mathrm{PLL}\left(\mathrm{diag}(\mathcal{W}^{LL}\mathbf{1}_n) - \mathcal{W}^{LL}\right) \\ J_{\bar{\omega}_L,\bar{\omega}_M} = -\omega_b\mathbf{K}_\mathrm{P}^\mathrm{PLL}\mathcal{W}^{LM}\end{cases} \tag{24}$$

where $\mathcal{W}^{LL} \in \mathbb{R}^{n\times n}$ and $\mathcal{W}^{LM} \in \mathbb{R}^{n\times m}$:
$i \in \{L_i : i = 1, ..n\}$:

$$\begin{cases}(\mathcal{W}^{LL})_{ir} = \begin{cases} g_{ir}, & r \in \{L_j : j = 1,..n, j \neq i\} \\ 0, & r = i\end{cases} \\ (\mathcal{W}^{LM})_{ir} = g_{ir} \quad r \in \{M_j, j = 1,..,m\}.\end{cases} \tag{25}$$

And $\mathcal{W}^{ML} \in \mathbb{R}^{m\times n}$ and $\mathcal{W}^{MM} \in \mathbb{R}^{m\times m}$:
$i \in \{M_i : 1,...,m\}$:

$$\begin{cases}(\mathcal{W}^{ML})_{ir} = k_{ir}, \quad r \in \{L_j : j = 1,...,n\} \\ (\mathcal{W}^{MM})_{ir} = \begin{cases} k_{ir}, r \in \{M_j : j = 1,...,m, j \neq i\} \\ 0, \quad r = i.\end{cases}\end{cases} \tag{26}$$

C. Proposed Contraction Metric and Contraction Region

We can see from (20)-(26) that the system Jacobian is composed of sub-matrices with hybrid structures. Some exhibit a Laplacian-like structure ($\mathbf{J}_{\bar{\omega}_L,\delta_L}$, $\mathbf{J}_{\bar{\omega}_M,\delta_M}$, $\mathbf{J}_{\bar{\omega}_L,\bar{\omega}_L}$), while others have a weighted adjacency matrix structure ($\mathbf{J}_{\bar{\omega}_L,\delta_M}$, $\mathbf{J}_{\bar{\omega}_M,\delta_L}$, $\mathbf{J}_{\bar{\omega}_L,\bar{\omega}_M}$). In addition, the sub-matrix $\mathbf{J}_{\bar{\omega},\bar{\omega}}$ is itself heterogeneous. To properly account for this hybrid structure, we begin by constructing a foundational state-dependent Laplacian matrix $\mathbf{L}(\mathbf{x}) \in \mathbb{R}^{n+m}$ as

$$\mathbf{L}_{(i,i)}(\mathbf{x}) = \sum\nolimits_{j\neq i} w_{ij}, \quad \mathbf{L}_{(i,i)}(\mathbf{x}) = -w_{ij} \tag{27}$$

where w_{ij} is an edge weight function defined by

$$w_{ij}(\mathbf{x}) = h\cdot\left[(1 - e^{(\delta_i-\delta_j)^2}) + k(1 - e^{(\bar{\omega}_i-\bar{\omega}_j)^2})\right] \tag{28}$$

where h is the coupling parameter. The first term represents angle coupling and the second term represents frequency coupling. The latter is scaled by a factor k to assign different weight to the frequency term in the composition of the edge weight.

To address the highly heterogeneous sub-matrix $\mathbf{J}_{\bar{\omega},\bar{\omega}}$, we define the coupling coefficient matrix to apply different scaling strengths to the GFL and GFM nodes via

$$\mathbf{C}_\omega = \mathrm{diag}(c_1, c_2, \ldots, c_{n+m}). \tag{29}$$

Based on the components of (27)-(29), the state-dependent augmentation metric is constructed as

$$\hat{\mathbf{M}}(\mathbf{x}) = \begin{bmatrix}\mathbf{H}_{11} & \mathbf{H}_{12} \\ \mathbf{H}_{21} & \mathbf{H}_{22}\end{bmatrix} \tag{30}$$

where

$$\begin{cases}\mathbf{H}_{11} = \mathbf{L}(\mathbf{x}), \quad \mathbf{H}_{12} = \mathbf{L}(\mathbf{x})/2 \\ \mathbf{H}_{21} = \mathbf{H}_{12}^T, \quad \mathbf{H}_{22} = \mathbf{C}_\omega^{1/2}\mathbf{L}(\mathbf{x})\mathbf{C}_\omega^{1/2}.\end{cases} \tag{31}$$

TABLE I
PARAMETERS OF MIXED GFM-GFL-INVERTER SYSTEM

Symbol	Description	Value
$(P_{L1}^{\mathrm{ref}},\ Q_{L1}^{\mathrm{ref}})$	GFL1's active and reactive power reference	(0.5, 0.42) p.u.
$(P_{L2}^{\mathrm{ref}},\ Q_{L2}^{\mathrm{ref}})$	GFL2's active and reactive power reference	(0.5, 0.174) p.u.
$(P_{M1}^{\mathrm{ref}},\ U_{M1}^{d})$	GFM1's active power and d-axis voltage reference	(0.5, 1.05) p.u.
$(P_{M2}^{\mathrm{ref}},\ U_{M2}^{d})$	GFM2's active power and d-axis voltage reference	(0.5, 1.05) p.u.
$(K_{\mathrm{P1}}^{\mathrm{PLL}},\ K_{\mathrm{I1}}^{\mathrm{PLL}})$	GFL1's PLL proportional and integral gains	(0.3, 40) p.u.
$(K_{\mathrm{P2}}^{\mathrm{PLL}},\ K_{\mathrm{I2}}^{\mathrm{PLL}})$	GFL2's PLL proportional and integral gains	(0.25, 35) p.u.
$(J_1,\ D_1)$	GFM1's VSG virtual inertia and damping coefficient	(1, 3) p.u.
$(J_2,\ D_2)$	GFM2's VSG virtual inertia and damping coefficient	(1.5, 2.5) p.u.

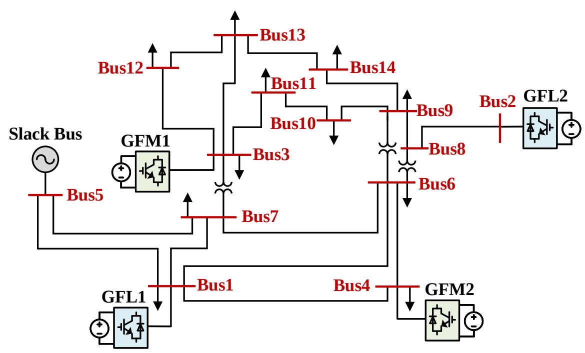

Fig. 4. Standard IEEE 14-Bus test system incorporated with mixed GFM and GFL inverters.

The final state-dependent contraction metric $\mathbf{M}(\mathbf{x})$ is then defined as

$$\mathbf{M}(\mathbf{x}) = \mathbf{P} + \hat{\mathbf{M}}(\mathbf{x}) \tag{32}$$

where $\mathbf{P}$ is a base constant, positive-definite matrix obtained by solving $\mathbf{J}^{\top}(\mathbf{x_s})\mathbf{P} + \mathbf{P}\mathbf{J}(\mathbf{x_s}) = -\mathbf{Q}$ for some positive-definite $\mathbf{Q}$ at the SEP ($\mathbf{x} = \mathbf{x_s}$).

Based on (18) and (32), the contraction region Ω is derived as

$$\Omega = \left\{ \mathbf{x} \in \mathbb{R}^{2(n+m)\times 1} \;\middle|\; \begin{array}{l} \mathbf{J}(\mathbf{x})^{\top}\mathbf{M}(\mathbf{x}) + \mathbf{M}(\mathbf{x})\mathbf{J}(\mathbf{x}) \\ + \dot{\mathbf{M}}(\mathbf{x}) \prec 0 \end{array} \right\}. \tag{33}$$

Compared with the constant metric $\mathbf{P}$, which is only optimal at the equilibrium point, the proposed state-dependent metric $\mathbf{M}(\mathbf{x})$ conforms to the system's nonlinear dynamics across the state space. This adaptability allows for a more flexible stability criteria, thereby yielding a larger estimated contraction region. At the time of fault clearance, we can therefore check if the system state satisfies the condition in (33). If it does, the system trajectory is confirmed to be within the contraction region Ω, guaranteeing its eventual convergence to the SEP.

IV. NUMERICAL RESULTS

The test system with mixed GFM and GFL inverters is shown in Fig. 4. It has the same layout and line impedances as the standard IEEE 14-Bus test system and the load is modeled as constant impedance load. The buses are renumbered and the SGs at Bus 1 $\sim$ Bus 4 are replaced by GFL and GFM inverters. The SG at Bus 5 is considered as the slack bus. The voltage magnitude of the slack bus U_g is set as 1 p.u. and the system base angular speed ω_b is 120π rad/s. Other parameters for the test system are listed in Table I.

A. Comparison of Derived Contraction Regions via Constant $\mathbf{P}$ and the Proposed State-Dependent $\mathbf{M}(\mathbf{x})$

Based on the condition in (33), Fig. 5 shows the phase-space slice of the derived contraction regions' of the test system at

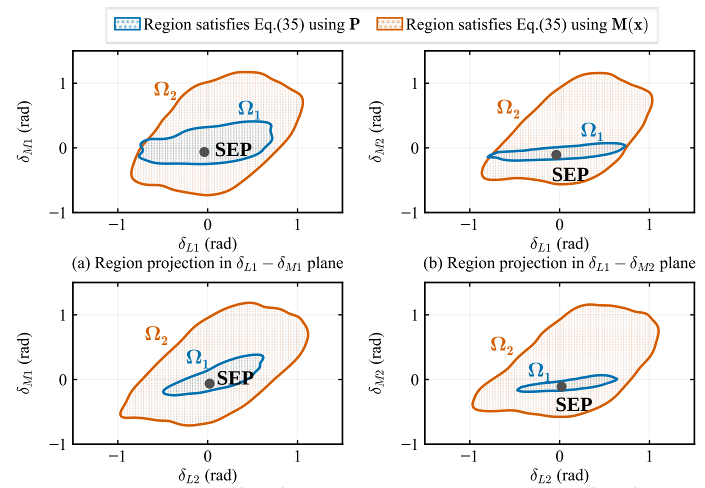

(a) Region projection in $\delta_{L1} - \delta_{M1}$ plane (b) Region projection in $\delta_{L1} - \delta_{M2}$ plane
(c) Region projection in $\delta_{L2} - \delta_{M1}$ plane (d) Region projection in $\delta_{L2} - \delta_{M2}$ plane

Fig. 5. Comparison of derived contraction region via constant $\mathbf{P}$ and proposed state-dependent $\mathbf{M}(\mathbf{x})$ on 2-D phase-planes.

TABLE II
UPPER AND LOWER LIMITS OF $\mathbf{\Omega_1}$ AND $\mathbf{\Omega_2}$ FOR THE FOUR INVERTERS

Inverters	$\mathbf{\Omega_1}$ range (rad)	$\mathbf{\Omega_2}$ range (rad)	η
GFL1	$(-0.742, 0.712)$	$(-0.833, 1.046)$	29.2%
GFL2	$(-0.470, 0.591)$	$(-0.955, 1.106)$	94.3%
GFM1	$(-0.242, 0.389)$	$(-0.722, 1.147)$	196.2%
GFM2	$(-0.192, 0.061)$	$(-0.546, 1.147)$	569.2%

$\bar{\omega_{\mathbf{L}}}, \bar{\omega_{\mathbf{M}}} = \mathbf{0}$. The region $\mathbf{\Omega_1}$ is obtained using the constant metric $\mathbf{P}$, which is calculated by solving $\mathbf{J}^{\top}(\mathbf{x_s})\mathbf{P} + \mathbf{P}\mathbf{J}(\mathbf{x_s}) = -\mathbf{Q}$ in MATLAB. In contrast, the region $\mathbf{\Omega_2}$ is obtained via the proposed state-dependent $\mathbf{M}(\mathbf{x})$ based on (27)-(32), where $h = 0.01$, $k = 0.5$ and $c_1, c_2 = 0.01$, $c_3, c_4 = 500$.

Table II summarizes the size of the contraction regions $\mathbf{\Omega_1}$ and $\mathbf{\Omega_2}$ for each inverter. To quantify the improvement of $\mathbf{\Omega_2}$ over $\mathbf{\Omega_1}$, Table II also includes the percentage increase in region size η_i. It is defined as $\eta_i = \frac{|\mathbf{\Omega_{2}}_i| - |\mathbf{\Omega_{1}}_i|}{|\mathbf{\Omega_{1}}_i|} \times 100\%$, where the subscript i denotes the specific inverter and $|\cdot|$ represents the measure of the region's size.

It can be observed from both Fig. 5 and Table II that the state-dependent metric yields larger contraction region compared to the constant metric. In particular, GFM2 inverter shows the most notable improvement with its contraction region expanded by 569.2%. Conversely, the enhancement for the GFL1 inverter is relatively minor, at only 29.2%. This outcome is consistent with the system configuration, where GFM2 inverter is more prone to instability due to its smaller damping coefficient. In contrast, GFL1 inverter, with well-tuned PLL parameters and close proximity to the slack bus, already exhibits strong inherent stability.

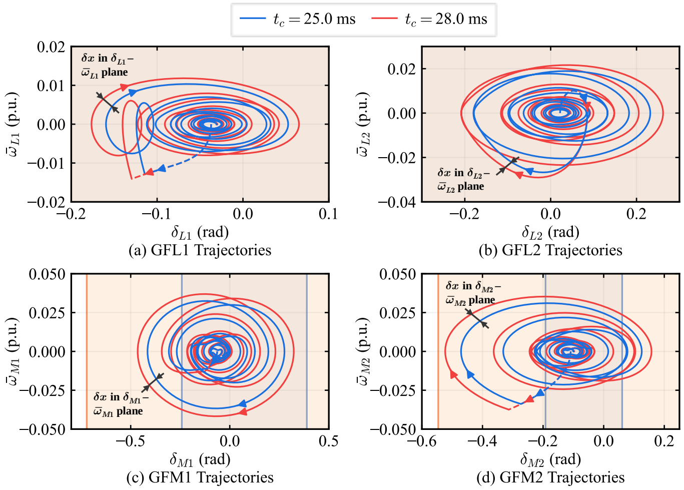

Fig. 6. System dynamics under U_g sag with $t_c = 25.0$ ms and 28.0 ms.

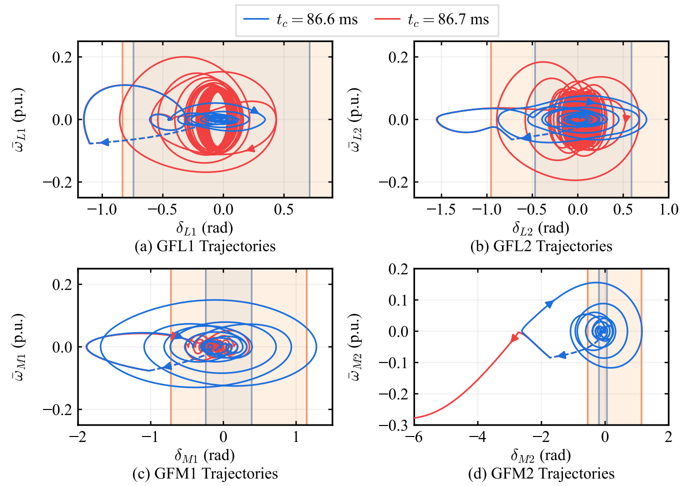

Fig. 7. System dynamics under U_g sag with $t_c = 86.6$ ms and 86.7 ms.

B. Verification of the Effectiveness and Conservativeness of Proposed Contraction Regions

To evaluate the system dynamics, large disturbances are introduced by reducing the infinite source voltage U_g to 0 p.u., followed by a restoration to 1.0 p.u. after a fault duration time of t_c seconds.

Fig. 6 compares the system dynamics under U_g sag with $t_c = 25.0$ ms and $t_c = 28.0$ ms. The light blue shaded area represents the range of $\boldsymbol{\Omega_1}$, and the light yellow shaded area corresponds to the range of $\boldsymbol{\Omega_2}$. In Fig. 6 (a) and (b), the plot windows are filled with the intersection of $\boldsymbol{\Omega_1}$ and $\boldsymbol{\Omega_2}$.

The post-fault trajectories in Fig. 6 demonstrate the effectiveness of the proposed contraction region. When the faults are cleared at $t_c = 25.0$ ms and $t_c = 28.0$ ms, both the red and blue trajectories are located within $\boldsymbol{\Omega_2}$. Subsequently, the trajectory displacement $\delta\mathbf{x}$ between them gradually decreases over time. The two trajectories eventually converge to the same SEP, confirming the effectiveness of $\boldsymbol{\Omega_2}$. Crucially, it can be seen from Fig. 6 (d) that, after fault clearance, the trajectories fall outside $\boldsymbol{\Omega_1}$ but remain within $\boldsymbol{\Omega_2}$. Their subsequent convergence further validates the improvement of the state-dependent metric $\mathbf{M}(\mathbf{x})$ over the constant metric $\mathbf{P}$.

Fig. 7 illustrates the system dynamics when the fault duration time is further increased to 86.6 ms and 86.7 ms. Under these two scenarios, the trajectories of GFL1, GFM1 and GFM2 inverters lie beyond both $\boldsymbol{\Omega_1}$ and $\boldsymbol{\Omega_2}$ at the moment of fault clearing, indicating instability as the entire trajectories of this 8-dimensional system extend beyond the derived contraction regions. Nevertheless, for $t_c = 86.6$ ms, the system trajectories still converge to the SEP, demonstrating the conservativeness and reliability of the proposed method. Furthermore, as shown for $t_c = 86.7$ ms, GFM1 inverter loses stability first, causing other inverters' trajectories to oscillate around the SEP with out convergence. This observation is consistent with the results in Table II, which indicate that $\mathbf{M}(\mathbf{x})$ provides the most significant improvement in contraction region estimation for the inverter that is most prone to instability.

V. Conclusions

This paper presents a contraction-theory-based framework for transient stability analysis of mixed GFM–GFL inverter systems. A state-dependent contraction metric is proposed based on the system's dynamic Jacobian matrix, from which the contraction region is derived. Simulation result verifies the effectiveness of the proposed method. Future work will focus on refining the metric structure to derive a less conservative estimate of the contraction region and incorporating inverter current limiting constraints.

979-8-3315-8138-1

References

[1] J. Matevosyan, J. MacDowell, N. Miller, B. Badrzadeh, D. Ramasubramanian, A. Isaacs, R. Quint, E. Quitmann, R. Pfeiffer, H. Urdal, T. Prevost, V. Vittal, D. Woodford, S. H. Huang, and J. O'Sullivan, "A future with inverter-based resources: Finding strength from traditional weakness," *IEEE Power and Energy Magazine*, vol. 19, no. 6, pp. 18–28, 2021.

[2] Y. Li, Y. Gu, and T. C. Green, "Revisiting grid-forming and grid-following inverters: A duality theory," *IEEE Transactions on Power Systems*, vol. 37, no. 6, pp. 4541–4554, 2022.

[3] R. Yang, G. Shi, X. Cai, C. Zhang, G. Li, and J. Liang, "Autonomous synchronizing and frequency response control of multi-terminal dc systems with wind farm integration," *IEEE Transactions on Sustainable Energy*, vol. 11, no. 4, pp. 2504–2514, 2020.

[4] G. Song, B. Cao, and L. Chang, "Review of grid-forming inverters in support of power system operation," *Chinese Journal of Electrical Engineering*, vol. 8, no. 1, pp. 1–15, 2022.

[5] C. Yang, L. Huang, H. Xin, and P. Ju, "Placing grid-forming converters to enhance small signal stability of pll-integrated power systems," *IEEE Transactions on Power Systems*, vol. 36, no. 4, pp. 3563–3573, 2021.

[6] X. Fu, M. Huang, S. Pan, and X. Zha, "Cascading synchronization instability in multi-vsc grid-connected system," *IEEE Transactions on Power Electronics*, vol. 37, no. 7, pp. 7572–7576, 2022.

[7] M. Li, X. Quan, Z. Wu, W. Li, L. Zhu, and Q. Hu, "Modeling and transient stability analysis of mixed-gfm-gfl-based power system," in *2021 IEEE Sustainable Power and Energy Conference (iSPEC)*, 2021, pp. 2755–2759.

[8] D. Lu, J. Yu, X. Lu, and J. Yu, "Synchronization stability of hybrid power systems integrated with grid-forming inverters and grid-following inverters," *CPSS Transactions on Power Electronics and Applications*, vol. 9, no. 4, pp. 405–415, 2024.

[9] X. Zhang, Z. Huang, Z. Wang, G. Li, L. Zheng, and S. Xia, "Transient stability analysis for hybrid gfm-gfl systems with current limit," in *2024 IEEE Power & Energy Society General Meeting (PESGM)*, 2024, pp. 1–5.

[10] N. Li, M. Zhang, X. Xu, S. Qiu, J. Li, and K. Ma, "Transient stability analysis and enhancement strategy of hybrid-converter system of grid-following and grid-forming," in *2024 China International Conference on Electricity Distribution (CICED)*, 2024, pp. 313–317.

[11] Y. Wang, Y. Cai, Y. Wang, H. Zheng, G. Ouyang, and Y. Xu, "Large disturbance stability analysis of system with paralleled grid following-voltage source converter and grid forming-voltage source converter," in *2024 IEEE 5th International Conference on Advanced Electrical and Energy Systems (AEES)*, 2024, pp. 349–354.

[12] Z. Aminzare and E. D. Sontagy, "Contraction methods for nonlinear systems: A brief introduction and some open problems," in *53rd IEEE Conference on Decision and Control*, 2014, pp. 3835–3847.

[13] G. Russo and M. di Bernardo, "Contraction theory and master stability function: Linking two approaches to study synchronization of complex networks," *IEEE Transactions on Circuits and Systems II: Express Briefs*, vol. 56, no. 2, pp. 177–181, 2009.

[14] E. M. Aylward, P. A. Parrilo, and J.-J. E. Slotine, "Stability and robustness analysis of nonlinear systems via contraction metrics and sos programming," *Automatica*, vol. 44, no. 8, pp. 2163–2170, 2008.

[15] R. M. Bora, B. S. Dey, and I. N. Kar, "On the contraction analysis of nonlinear system with multiple equilibrium points," *arXiv preprint arXiv:2502.14242*, 2025. [Online]. Available: https://doi.org/10.48550/arXiv.2502.14242

[16] M. Yilmaz and F. K. Bayat, "Contraction region analysis for power systems," in *2019 IEEE Texas Power and Energy Conference (TPEC)*, 2019, pp. 1–6.

[17] H. K. Khalil, *Nonlinear Systems*, 3rd ed. Upper Saddle River, NJ: Prentice Hall, 2002.